

MASSIVE STAR-FORMING HOST GALAXIES OF QUASARS ON SLOAN DIGITAL SKY SURVEY STRIPE 82

YOSHIKI MATSUOKA^{1,2}, MICHAEL A. STRAUSS¹, TED N. PRICE III^{1,3}, AND MATTHEW S. DIDONATO^{1,4}

Draft version October 13, 2018

ABSTRACT

The stellar properties of about 800 galaxies hosting optically luminous, unobscured quasars at $z < 0.6$ are analyzed. Deep co-added Sloan Digital Sky Survey (SDSS) images of the quasars on Stripe 82 are decomposed into nucleus and host galaxy using point spread function and Sérsic models. The systematic errors in the measured galaxy absolute magnitudes and colors are estimated to be less than 0.5 mag and 0.1 mag, respectively, with simulated quasar images. The effect of quasar light scattered by the interstellar medium is also carefully addressed. The measured quasar-to-galaxy ratio in total flux decreases toward longer wavelengths, from ~ 8 in the u band to ~ 1 in the i and z bands. We find that the SDSS quasars are hosted exclusively by massive galaxies (stellar mass $M_{\text{star}} > 10^{10} M_{\odot}$), which is consistent with previous results for less luminous narrow-line (obscured) active galactic nuclei (AGNs). The quasar hosts are very blue and almost absent on the red sequence, showing stark contrast to the color–magnitude distribution of normal galaxies. The fact that more powerful AGNs reside in galaxies with higher star-formation efficiency may indicate that negative AGN feedback, if it exists, is not concurrent with the most luminous phase of AGNs. We also find positive correlation between the mass of supermassive black holes (SMBHs; M_{BH}) and host stellar mass, but the $M_{\text{BH}} - M_{\text{star}}$ relation is offset toward large M_{BH} or small M_{star} compared to the local relation. While this could indicate that SMBHs grow earlier than do their host galaxies, such an argument is not conclusive, as the effect may be dominated by observational biases.

Subject headings: galaxies: active — galaxies: evolution — galaxies: nuclei — galaxies: stellar content
— quasars: general — quasars: supermassive black holes

1. INTRODUCTION

The interrelation between supermassive black holes (SMBHs) and their host galaxies is a central issue of astrophysics today. The unexpectedly tight correlation between the mass of SMBHs (M_{BH}) and the velocity dispersion (σ_*) or mass of their host bulges (e.g., Dressler 1989; Kormendy 1993; Magorrian et al. 1998; Merritt & Ferrarese 2001; McLure & Dunlop 2002; Häring & Rix 2004; Gültekin et al. 2009) suggests that the two coevolve, or at least strongly influence each other. The observed scatter in the $M_{\text{BH}} - \sigma_*$ relation is explained almost solely by measurement errors (Ferrarese & Merritt 2000; Gebhardt et al. 2000). Such a tight correlation suggests a fine-tuning process, perhaps a combination of internal physics within galaxies or dark halos, and mass averaging via successive mergers as predicted in hierarchical galaxy formation models (see the recent review by Kormendy & Ho 2013, and references therein). Among the possible physical processes that can drive the co-evolution of SMBHs and host galaxies, the most compelling today is negative feedback caused by active galactic nuclei (AGNs; e.g., Ciotti & Ostriker 2007; Ostriker et al. 2010; Fabian 2012). It has been suggested that the energy input from AGNs, which may have been triggered along with active

starbursts by interactions/mergers of gas-rich galaxies (e.g., Barnes & Hernquist 1991), could quench star formation in the host galaxies by expelling the cold gas from galaxies (quasar-mode feedback; e.g., Di Matteo et al. 2005; Springel et al. 2005) and/or heating the gas in dark halos (radio-mode feedback; e.g., McNamara & Nulsen 2007, and references therein).

The AGN feedback model is gaining broad support in part because it may give a solution to longstanding problems in standard galaxy formation models (e.g., Somerville et al. 2008); for example, it is currently the most compelling process to reconcile the very different shapes of the dark halo mass function predicted in the Λ CDM cosmology and the observed galaxy stellar mass function, especially at the high mass end (e.g., Bower et al. 2006; Croton et al. 2006; Davé et al. 2011; Choi & Nagamine 2011). In addition, recent observations of AGN-driven gas outflows (e.g., Nesvadba et al. 2006; Feruglio et al. 2010; Greene et al. 2011; Cano-Díaz et al. 2012) and extended emission-line regions photoionized by AGNs (e.g., Fu & Stockton 2009; Husemann et al. 2010; Greene et al. 2011; Matsuoka 2012; Keel et al. 2012; Liu et al. 2013a,b) strongly suggest that AGNs have significant impact on their host galaxies. However, all these arguments are only circumstantial evidence for the putative AGN feedback. Stellar populations of AGN hosts are expected to provide a key piece of information, since the end effect of AGN feedback should appear in stellar properties.

One of the earliest studies of the stellar populations of quasar hosts was presented by Boroson & Oke (1982) who found that the off-nucleus spectrum of

¹ Princeton University Observatory, Peyton Hall, Princeton, NJ 08544, USA

² National Astronomical Observatory of Japan, Mitaka, Tokyo 181-8588, Japan

³ Eastdil Secured, 40 West 57th Street, New York, NY 10019, USA

⁴ Haddonfield Memorial High School, Haddonfield, NJ 08033, USA

the quasar 3C 48 was dominated by hot young stars. Kotilainen & Ward (1994) analyzed imaging data of nearby Seyfert 1s and found that near-infrared colors of their hosts are similar to those of moderately luminous starburst galaxies and that host luminosity is positively correlated with AGN luminosity. Rönnback et al. (1996), studying radio-loud and radio-quiet quasars at $0.4 < z < 0.8$, discovered that the quasars reside in luminous galaxies whose optical colors are consistent with late-type spirals and irregular galaxies. More recent studies have benefited greatly from the advent of *Hubble Space Telescope* (*HST*), since resolution of the host galaxies from extremely bright nucleus is the key to accurate quantification of host properties. Bahcall et al. (1997) showed that luminous quasars reside preferentially in luminous galaxies with diverse morphology. The excess detection of close companions, tidal features, and dense surrounding environments led them to conclude that gravitational interactions are important in triggering quasar activity. In addition, Kirhakos et al. (1999) found that quasar hosts are 0.5–1.0 mag bluer in $V - I$ than normal galaxies – a sign of active star formation connected to quasars. On the other hand, McLure et al. (1999) claimed that quasars are almost exclusively hosted by massive ellipticals (the mean half-light radius was found to be ~ 10 kpc) with $R - K$ colors consistent with old stellar populations. At least part of the discrepancy between the Bahcall et al. and McLure et al. results may be attributed to the different filter choices and different modeling methods. At higher redshifts up to $z \sim 3$, Jahnke et al. (2004) showed that blue ultraviolet colors of host galaxies indicate recent starburst or ongoing star formation activity, which was later reconfirmed using spatially decomposed spectra by Jahnke et al. (2007). A similar result in terms of enhanced blue light in quasar host galaxies was also obtained by Sánchez et al. (2004).

Recently, the Sloan Digital Sky Survey (SDSS; York et al. 2000) has revolutionized this field via detection of large samples of narrow-line AGNs with low (e.g., Kauffmann et al. 2003; Hao et al. 2005) and high (e.g., Zakamska et al. 2003; Reyes et al. 2008) luminosity. In these obscured populations, the host galaxies are much more easily observed than in unobscured objects (e.g., Zakamska et al. 2006; Liu et al. 2009). Obscured AGNs have also been investigated with X-ray observations at redshifts up to $z = 1$ and above (e.g., Nandra et al. 2007; Georgakakis et al. 2008; Silverman et al. 2008). Overall, the above studies are consistent in finding that obscured AGNs reside preferentially in massive galaxies whose colors are systematically bluer than those of normal galaxies with similar stellar mass. Of particular note is the highest AGN fraction in the green valley of the color-magnitude diagram (CMD) as claimed by some authors (e.g., Schawinski et al. 2010), which is consistent with (but not necessarily indicative of) a scenario in which AGNs are responsible for transforming blue star-forming galaxies into red quiescent galaxies. AGNs found in post-starburst galaxies (e.g., Brotherton et al. 1999, 2002) may represent this stage. There are also some indications that higher-luminosity AGNs reside in bluer galaxies (e.g., Kauffmann et al. 2003; Salim et al. 2007), which seems to contradict the idea that negative AGN feedback on star formation is concurrent with the period of highest nuclear activity. At the same time, detailed

analyses of obscured quasars have revealed the presence of significant amount of scattered quasar light in host galaxies (Zakamska et al. 2006; Liu et al. 2009). If not handled properly, this could result in a serious bias in which the hosts of more luminous AGNs are observed to be bluer, since the AGN spectral energy distribution is usually much bluer than that of starlight.

Despite the above intense efforts, one of the biggest pieces of the puzzle still missing is the general nature of galaxies hosting “classical” quasars, i.e., hosts of optically-luminous unobscured quasars. Since different types of AGN may have different hosts and may play different roles in galaxy evolution (e.g., Hickox et al. 2009), it is critically important to study the hosts of all types. The simplest AGN unification model (see the review article of Antonucci 1993) assumes that unobscured (type-1) and obscured (type-2) AGNs are intrinsically the same except for the orientation of the obscuring material relative to the observer’s line-of-sight, but the actual situation is likely to be more complicated. For example, obscured AGNs are more likely to be embedded in dusty circumnuclear environments than are unobscured ones (Elitzur 2012). In the merger-driven evolution scenario of galaxies and SMBHs described by Hopkins et al. (2006), the dusty starburst/AGN phase (sometimes observed as ultra-luminous infrared galaxies, ULIRGs) precedes the dust-free phase observed as optically luminous quasars (see also Sanders et al. 1988). If this is the case, then obscured and unobscured AGNs would represent different stages of galaxy evolution.

In this work, we present a statistical analysis of host galaxies of luminous unobscured quasars at low redshifts ($z < 0.6$). By making use of the deep co-added SDSS images on Stripe 82 on the celestial equator, we successfully decompose host galaxies from bright quasar nuclei and investigate the stellar properties of more than 800 sources. This paper is organized as follows. The data and sample are presented in Section 2. Section 3 describes the method of analysis we use to decompose the source images into quasar nuclei and host galaxies. The main results appear in Section 4. Then, in Section 5, we discuss the implication of the results as well as the possible drawbacks of the present analysis, including quasar light contamination in measured host brightness. A summary follows in Section 6. The cosmological parameters of $H_0 = 70 \text{ km s}^{-1}$, $\Omega_M = 0.3$, and $\Omega_\Lambda = 0.7$ are assumed throughout the paper. All the magnitudes are presented on the AB system.

2. DATA AND SAMPLE SELECTION

The data and catalogs used in this work were obtained through a set of SDSS projects; SDSS-I (York et al. 2000), the SDSS-II Supernova Survey (Frieman et al. 2008), and the SDSS-III Baryon Oscillation Spectroscopic Survey (BOSS; Dawson et al. 2013). SDSS uses a dedicated 2.5 m telescope (Gunn et al. 2006) at Apache Point Observatory, New Mexico. The telescope is equipped with a mosaic CCD camera (Gunn et al. 1998) and twin multi-object fiber spectrographs developed for SDSS-I and upgraded for BOSS (Smee et al. 2013). We make use of the deep stacked images of Stripe 82, the 2.5° -wide (in declination) stripe on the celestial equator from about 20^{h} to 6^{h} (in right ascension). Those images have been created by co-adding multiple scans of

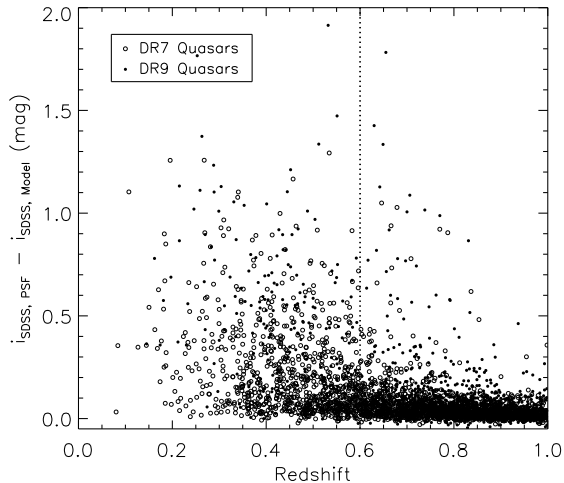


Figure 1. Difference between the two sets of SDSS i -band magnitudes, $i_{\text{SDSS,PSF}}$ (PSF magnitudes) and $i_{\text{SDSS,Model}}$ (model magnitudes), of the quasars on Stripe 82 as a function of redshift. The open and filled circles represent the DR7 and DR9 quasars, respectively. The dotted line shows the redshift limit ($z = 0.6$) applied in this work.

the stripe obtained through SDSS-I and the Supernova Survey (Annis et al. 2011). Typically about 20 scans contribute to each piece of the sky, giving an effective exposure time of ~ 1000 s. The 50% completeness limits for point sources are (23.6, 24.6, 24.2, 23.7, 22.3) mag in the (u , g , r , i , z) bands, which are approximately 2 mag deeper than a single SDSS exposure. The mean full widths at half maximum of the point spread functions (PSFs) are $\sim 1''.3$ in the u , g bands and $\sim 1''.1$ in the r , i , and z bands.

The sample is selected from the fifth SDSS quasar catalog (Schneider et al. 2010) based on data release (DR) 7 (Abazajian et al. 2009) and the first BOSS quasar catalog (Pâris et al. 2012) based on DR9 (Ahn et al. 2012). The former catalog contains quasars with $M_i < -22$ mag, while the latter contains fainter objects down to $M_i(z=2) = -20.5$ mag (corresponding to $M_i = M_i(z=0) \simeq -19.9$ mag; Richards et al. 2006). In order to have a rough estimate of the resolved fraction as a function of redshift, we check the difference between the two sets of SDSS magnitudes, the PSF magnitudes ($m_{\text{SDSS,PSF}}$) and the model magnitudes ($m_{\text{SDSS,Model}}$), of those quasars on Stripe 82. Since $m_{\text{SDSS,PSF}}$ and $m_{\text{SDSS,Model}}$ are designed to measure the total brightness of unresolved and resolved sources, respectively, the difference between the two is larger for more extended sources. Since a good fraction of the quasars seem to be resolved up to $z \sim 0.6$ as plotted in Figure 1, we decided to apply the present analysis to the objects at $z < 0.6$. After removing the objects with nearby bright sources (the rejection criteria are detailed in the next section), we have 1041 (802 DR7 and 239 DR9) quasars which constitute our initial sample. Those objects have a variety of SDSS target flags. Most of them have been targeted as quasar or galaxy targets for various reasons, based on colors, extendedness, variability, and/or detection at other wavelengths. The total number of objects targeted as quasar candidates is roughly equal to those targeted as galaxies in our sample. We show the distribution of redshifts and absolute mag-

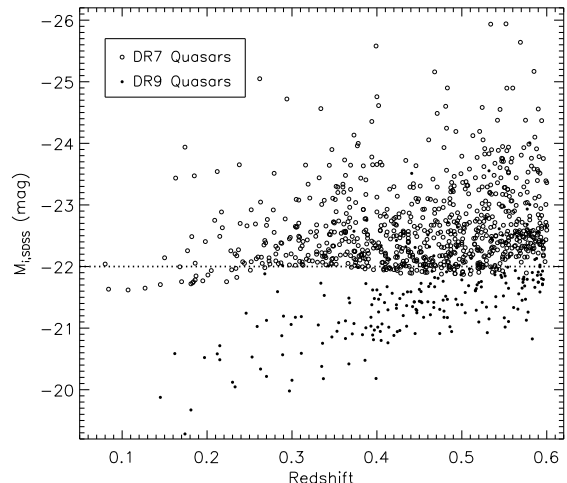


Figure 2. Redshifts and absolute magnitudes $M_{i,\text{SDSS}}$ of the quasar sample (open circles: DR7 quasars, filled circles: DR9 quasars). The dotted line represents the luminosity threshold of the original DR7 quasar selection (Schneider et al. 2010).

nitudes $M_{i,\text{SDSS}}$ ⁵ of the initial sample in Figure 2. The k -correction has been applied following Richards et al. (2006). Most of the objects are at $z > 0.3$; the median redshift is $\langle z \rangle = 0.47$. Note that some of the DR7 quasars fall below the luminosity threshold originally applied by Schneider et al. (2010) because of the slightly different k -corrections applied. We could select more low-luminous AGNs at low redshifts from the SDSS main galaxy sample (Strauss et al. 2002), but we defer this to future work.

We additionally retrieve the nuclear properties ([O III] $\lambda 5007$ line luminosity, SMBH mass, and Eddington ratio) of the DR7 quasars from Shen et al. (2011). Most of the properties were estimated based on the quasar emission lines contained in the SDSS spectral data. All the SMBH masses used in this work were derived from the single-epoch measurement of $\text{H}\beta$, which is believed to be more reliable than any other known single-epoch estimators (Shen & Liu 2012; Shen 2013). The following results and arguments related to those nuclear properties include only the DR7 quasars.

3. IMAGE ANALYSIS

3.1. Measurements of Host Galaxy Brightness

We work directly on co-added SDSS images created by Annis et al. (2011). We show three-color composite images of one of the quasars in Figure 3 as an illustration. The analysis is carried out separately for images of the same object taken through different filters. In order to avoid any additional complexity and/or systematic uncertainty arising from source deblending, we reject those objects whose images are possibly affected by nearby sources. If a bright source (< 15 mag in any of the u , g , r , i , and z bands) is present in the 100 pixel \times 100 pixel ($40'' \times 40''$) image cutout centered on a quasar, then the quasar is thrown away. For a fainter nearby source of magnitude m found in the image cutout, all the pixels within $10.0 - 0.5(m - 15.0)$ pixels of the source

⁵ Hereafter i_{SDSS} denotes the SDSS PSF magnitude ($= i_{\text{SDSS,PSF}}$) taken from the original quasar catalogs and corrected for Galactic extinction from Schlegel et al. (1998). $M_{i,\text{SDSS}}$ is the absolute magnitude calculated from i_{SDSS} with a k -correction to $z = 0$.

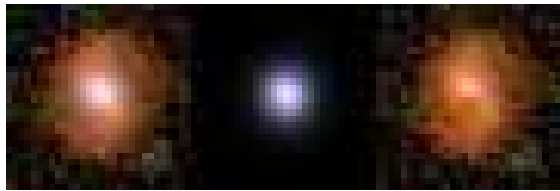


Figure 3. Three-color composite images of SDSS J002450.50+003447.7 at $z = 0.524$. The SDSS i , r , g -band images were used to create the red–green–blue composites with the recipe of Lupton et al. (2004). Left: the original image, middle: the best-fit PSF model, right: the PSF-subtracted image. The same flux scaling is applied for the three panels so that the brightness and colors can be directly compared by eye. The size of each panel corresponds to $100 \text{ kpc} \times 100 \text{ kpc}$ at the object’s distance.

(empirically determined to be large enough to avoid any significant light contamination) are excluded from the fitting procedure described below. We check the fraction of the rejected pixels around each quasar, and if the fraction exceeds 0.5 in any one of the five annuli centered on the quasar with inner/outer radii of $n/n + 1$ pixels ($n = 0, 1, 2, 3, 4$), then the quasar is excluded from the sample. The above criteria reduce the number of the quasars by about 6 % and result in our initial sample of 1041 objects. Although sky subtraction has been already done for the co-added images, we found that the background values around some of the quasars have positive or negative offset levels. This may be due to residual sky subtraction issues in SDSS photometric processing, as described in Abazajian et al. (2009). We measure this local offset by iterative σ -clipping within the $100 \text{ pixel} \times 100 \text{ pixel}$ image cutout, and correct for it.

We fit the azimuthal-average radial profile of each object, $I_{\text{obj}}(R)$, with an optimized combination of the PSF and the Sérsic (1968) function (a concise reference to the Sérsic function is found in Graham & Driver 2005). We do not use a more complicated procedure like two-dimensional fitting in this study, partly due to the image quality of SDSS (which is significantly worse than those of *HST* observations), and partly because we are interested only in total brightness (not in the exact values of structural parameters). The pixel coordinates of the quasar centroid are obtained from the celestial coordinates listed in the original quasar catalogs and the astrometric calibration stored in the header of the co-added images (fpC frames). The PSF at the position of each source in each band is extracted from the relevant SDSS measurements (contained in the `psField` products); in the SDSS data processing, the PSF in each CCD frame was determined from 15–20 bright stars using the Karhunen–Loève transform technique (Lupton et al. 2001), which was then synthesized into the PSF of a co-added image with suitable weighting (Annis et al. 2011). The amplitude I_{PSF} is the only adjustable parameter associated with the central point source in our analysis. The Sérsic function has the form

$$I(R) = I_e \exp \left(-b_n \left[\left(\frac{R}{R_e} \right)^{\frac{1}{n}} - 1 \right] \right), \quad (1)$$

where R_e is the effective radius enclosing half of the total light and I_e is the intensity at the radius $R = R_e$. The Sérsic index n describes the overall profile shape. The constant b_n is uniquely determined once R_e and n are

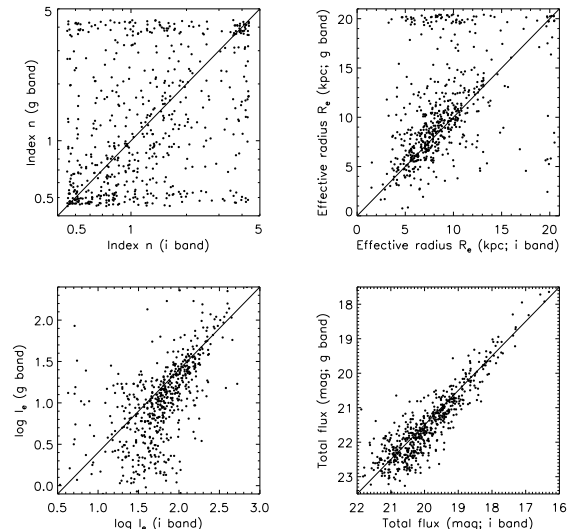


Figure 4. Cross-comparison between the g and i bands of the best-fit parameters n (top left), R_e (top right), $\log I_e$ (bottom left) of the Sérsic profile as well as the integrated flux out to $R = 30 \text{ kpc}$ (F_{Galaxy} ; bottom right). Small random offsets have been applied to improve visibility. The typical fitting uncertainty is $\sigma_{\log n} = 0.25$, $\sigma_{R_e} < 1.0 \text{ kpc}$ (i.e., less than the grid interval), $\sigma_{\log I_e} = 0.13$, and $< 0.1 \text{ mag}$ for the integrated flux. The solid lines in the top two panels represent the locus where the results of the two bands are identical, while those in the bottom panels represent the approximate mean color of $g - i = 1.5$.

given, so that R_e meets its definition as the half-light radius. Therefore the fitting procedure involves four free parameters of two profile components; I_{PSF} (PSF) and I_e , n , R_e (the Sérsic function). The Sérsic function is convolved with the corresponding PSF to accommodate the effect of seeing. The object’s radial profile $I_{\text{obj}}(R)$ is measured in bins one pixel wide, i.e., in annuli with the inner/outer radii of $n/n + 1$ ($n = 0, 1, 2, \dots$) pixels centered on the object, out to the pixel scale corresponding to 30 kpc at the object’s distance. The associated error is estimated from the root mean square (rms) of the data values in each bin. Any bins in which the mean flux is less than three times the associated error are excluded from the analysis. We do not perform the analysis when there are less than five profile points available. We keep track of all the discarded objects in each band throughout the fitting procedure for later discussion.

In order to minimize parameter degeneracy and/or physically unreasonable regions of parameter space, we carry out the fitting analysis in two steps as follows. The first step is conducted in the i band to determine the values of n and R_e of each galaxy. The choice of i band is made since the quasar-to-galaxy contrast is in general lower at longer wavelength (i.e., galaxies are redder than quasars), making the galaxy component more visible, and the SDSS signal-to-noise ratio is much better in the g , r , and i bands than in the other two bands. Also, the seeing tends to be better at longer wavelengths. I_{PSF} is tentatively calculated by assuming that the source profile has negligible contribution from the Sérsic component at $R < 2 \text{ pixel}$. Then we subtract the PSF from the source and fit the residual profile at $R > 2 \text{ pixel}$ with the Sérsic function. We discard those objects whose residual flux is less than 10 % of the subtracted PSF flux. The Sérsic amplitude I_e is varied freely, while n and R_e are changed among values on a pre-fixed grid; n can take

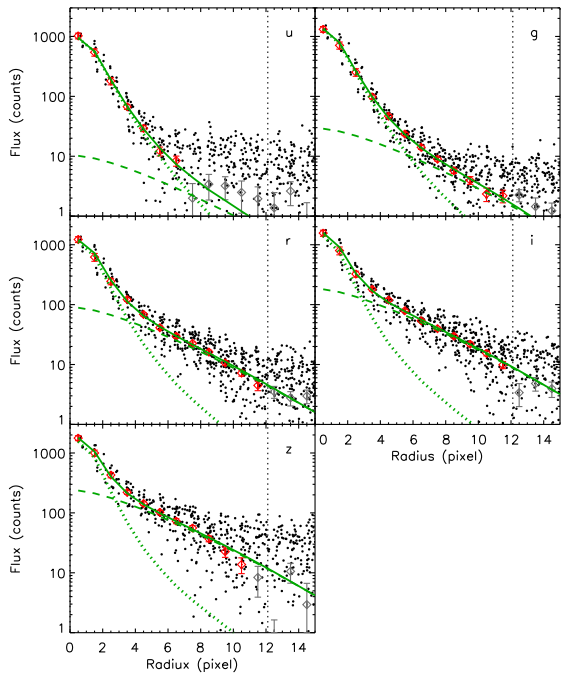


Figure 5. Fitting results for the quasar SDSS J002450.50+003447.7 at $z = 0.524$ (the same object as shown in Figure 3) in the u (top left), g (top right), r (middle left), i (middle right), and z (bottom) bands. The dots correspond to individual CCD pixels around the quasar. The diamonds represent the azimuthally averaged radial profile; those used in the fitting are in red, while those discarded for quality reasons (see text) are in gray. The best-fit profiles are shown by the green lines; the PSF (dotted lines) and the Sérsic (dashed lines) components as well as their sum (solid lines). The vertical dotted lines show the pixel scale corresponding to 30 kpc at the object’s distance.

ten values logarithmically stepped from 0.5 to 4.0, and R_e can take twenty values linearly stepped from 1 to 20 kpc. We also conducted the above procedure in the g band and cross-compared the results with those in the i band, as shown in Figure 4. Clearly, the total fluxes contained in the Sérsic functions of the two bands correlate fairly well despite the presence of scatter in intrinsic galaxy color, while none of the individual free parameters n , R_e , or I_e shows better correlation. This suggests that our approach works well to reproduce the overall flux of the non-PSF component, even if the individual parameters are not constrained very accurately.

Second, we use the n and R_e values determined above (in the i band) and fit the combined PSF plus Sérsic function to the observed profile in each band by varying I_{PSF} and I_e simultaneously. We show one of the good fitting results in Figure 5 to illustrate our procedure; this is the same object as shown in Figure 3. The distribution of the reduced χ^2 values of the best fits peaks around 1 and is fairly close to the expected χ^2 distribution in all the five bands, as shown in Figure 6, suggesting that our model reproduces the observed source profiles reasonably well. We measure the galaxy flux (F_{Galaxy}) by integrating the best-fit Sérsic function out to $R = 30$ kpc and the quasar flux (F_{Quasar}) by integrating the PSF. These are corrected for the Galactic extinction taken from Schlegel et al. (1998). Those fitting results whose estimated errors in galaxy flux exceed 2.5 mag are discarded; they are at the tail of the error distribution, as most (about 70 % in the u band and more than 95 %

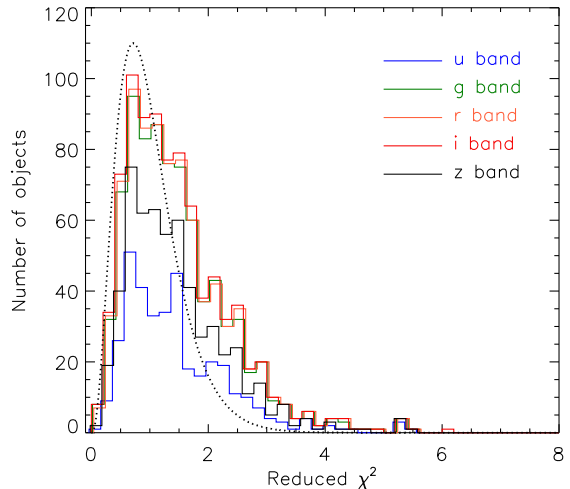


Figure 6. Distributions of the reduced χ^2 values of the best fits. The blue, green, orange, red and black solid lines represent the u , g , r , i , and z bands, respectively. They are slightly offset from each other to improve visibility. The dotted line represents the expected χ^2 distribution (arbitrary scaled); the mean degree of freedom in the i band is used for the calculation).

in the g , r , i , z bands) of the objects with successful fits have galaxy flux errors of less than 0.5 mag.

For robust estimates of the galaxy k -correction and (stellar) mass-to-light ratio, we need to know the spectral energy distribution of each galaxy reasonably well. To this end, we require that the fitting results be available in at least three of the g , r , i , and z bands (this is called the “good-fit criterion” hereafter). We decided not to consider the u -band results for further analysis, since the galaxy component is not visible in many objects in this band due to low signal-to-noise ratio and high quasar-to-galaxy contrast. Figure 7 shows the number statistics of the initial sample and the fraction of the good-fit objects as a function of redshift and magnitude. The good-fit fraction decreases toward higher redshift and fainter magnitude, as expected, dropping to nearly 50% at $z = 0.6$, $i_{\text{SDSS}} = 20$ mag, or $M_{i,\text{SDSS}} = -20$ mag. The most luminous objects also tend to fail in the fitting because of the highest quasar-to-galaxy contrasts, but they are only a small fraction of the whole sample. In total, 802 quasars or 77 % of the initial sample meet the good-fit criterion. For these objects, we estimate the absolute magnitudes and mass-to-luminosity ratios of the host galaxies using the public k -correction code `kcorrect`, version 4.2 (Blanton & Roweis 2007). Throughout this paper we express the absolute magnitudes of the host galaxies in the SDSS g and i bands shifted to $z = 0.3$, which are denoted as $^{0.3}M_g$ and $^{0.3}M_i$. The color in these shifted bandpasses is $^{0.3}(g - i) \equiv ^{0.3}M_g - ^{0.3}M_i$. Roughly speaking, the bandpasses of $^{0.3}M_g$ and $^{0.3}M_i$ are close to those of the original SDSS u and r bands, respectively. The median conversion factor from $^{0.3}M_i$ to stellar mass M_{star} is found to be $\log(M_{\text{star}}/M_{\odot}) + 0.4 ^{0.3}M_i = 2.09$. Note that quasar absolute magnitudes are always k -corrected to $z = 0$ in this work.

3.2. Systematic Errors

Here we estimate systematic errors arising from the above procedure with simulated quasar images. We first

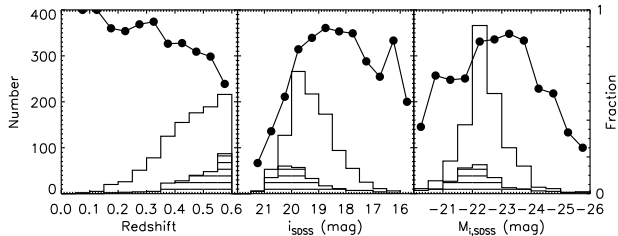


Figure 7. Number of quasars in the initial sample as a function of redshift (left), i_{SDSS} (middle), and $M_{i,\text{SDSS}}$ (right) are shown by the histograms. The hatched histograms represent the objects that fail to meet the good-fit criterion. The good-fit fractions are shown by the dots connected by the solid lines (the scale is shown on the right axis).

select about 1300 galaxies on Stripe 82 from the SDSS DR10 (Ahn et al. 2013) database, in such a way that they are distributed fairly uniformly in the space of redshift and $g - i$ color in the range $0.1 < z < 0.6$ and $0 < g - i < 4$. Although most of the DR10 galaxies with spectroscopic redshifts at $z > 0.3$ are red, with passive stellar population, we were able to find a sufficient number of blue galaxies that cover the redshift and color distributions of the real quasar hosts (see below). The galaxies (with SDSS model magnitudes $m_{\text{gal,orig}}$) are extracted from the same imaging data as used in the above analysis, and their flux scales are reduced so that the resultant galaxy magnitudes become $m_{\text{gal}} = m_{\text{gal,orig}} + \Delta m$ where $\Delta m = 0, 1, 2, 3, 4$ mag. Since this procedure also reduces background noise, we add additional random Gaussian noise that restores the amplitude of the original background fluctuation. Next we randomly pick a bright star from the SDSS Stripe 82 standard star catalog (Ivezić et al. 2007) for each of the above galaxies, and add its image to the dimmed galaxy image by aligning the source centroids. In order to reproduce a range of quasar-to-galaxy contrast, the stellar flux is reduced to $m_{\text{star}} = m_{\text{gal}} + \Delta m_{\text{contrast}} + \Delta m_{\text{random}}$ where $\Delta m_{\text{contrast}} = -3, -2, -1, 0, 1, 2$ mag and Δm_{random} is a random variable between -0.5 and $+0.5$ mag. These superimposed galaxy + star images comprise our synthesized quasar images, which are processed through the same analysis algorithm as used for the real quasar sample. For simplicity in the rest of this subsection, we denote the input and output galaxy magnitudes by m_0 ($= m_{\text{gal}}$ above) and m , respectively, and the input and output quasar magnitudes by m_0^{QSO} ($= m_{\text{star}}$ above) and m^{QSO} , respectively.

Figure 8 shows the success rate of the fitting procedure for the simulated quasars (the fraction of the simulated quasars meeting the good-fit criterion defined in the previous subsection) on a few projection planes of the parameter space. The distribution of real quasars is superposed. The success rate is most strongly dependent on galaxy magnitude; the fitting tends to fail for galaxies fainter than $i_0 \sim 21$ mag. On the other hand, it is less dependent on redshift or galaxy color $g_0 - i_0$ at fixed galaxy magnitude. For faint galaxies with $i_0 > 20$ mag, the success rate is higher at higher quasar-to-galaxy contrast, because the brighter quasar light helps to pass the signal-to-noise ratio cut in the analysis algorithm. Finally, on the galaxy CMD of $^{0.3}M_{i,0}$ and $^{0.3}(g - i)_0$, the success rate decreases toward the lower-luminous and redder region where galaxies have the lowest apparent brightness

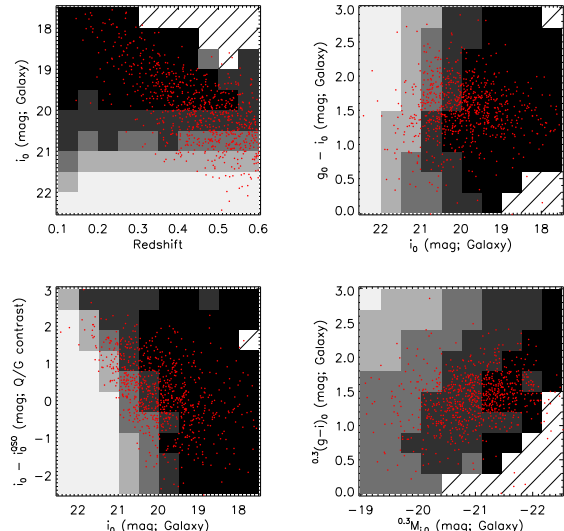


Figure 8. Success rate of the fitting procedure as a function of redshift and magnitude i_0 (top left), magnitude i_0 and color $g_0 - i_0$ (top right), magnitude i_0 and quasar-to-galaxy contrast $i_0 - i_0^{\text{QSO}}$ (bottom left), and absolute magnitude $^{0.3}M_{i,0}$ and color $^{0.3}(g - i)_0$ (bottom right). The rate decreases from > 0.8 in the black cells to < 0.2 in the lightest grey cells, while the hatched area shows where there are less than ten simulated galaxies in a cell. The red dots represent our real quasars with successful fits.

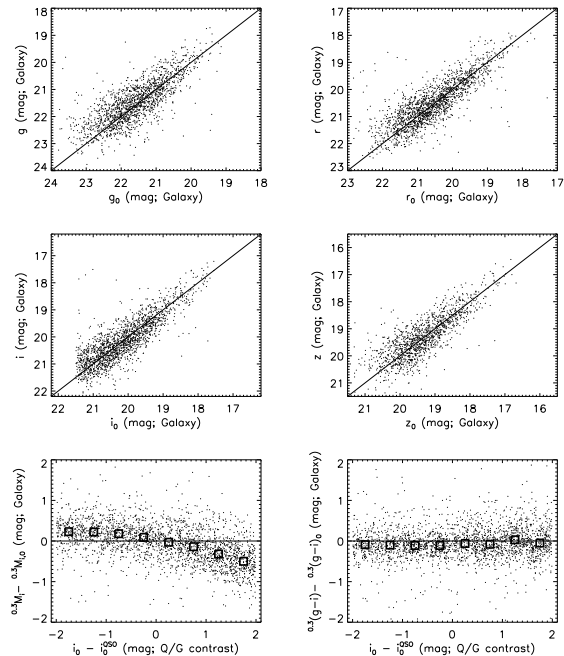


Figure 9. Top and middle panels: comparisons of the input and output galaxy magnitudes in the g (top left), r (top right), i (middle left), and z (middle right) bands from our simulations of galaxy-star superpositions. The truncation of the i_0 distribution at 21.5 mag is caused by the selection criteria of the simulated quasars used for these comparisons (see text). Bottom panels: differences between the input and output values of $^{0.3}M_i$ (bottom left) and $^{0.3}(g - i)$ (bottom right) as a function of the quasar-to-galaxy contrast $i_0 - i_0^{\text{QSO}}$ (dots). The squares represent median values in bins. In all the panels, the solid lines represent the locus where the input and output values are equal.

in the optical bands. We suspect that the real quasars that fail to meet the good-fit criterion, which comprise $\sim 23\%$ of the initial sample, fall in those particular regions of the parameter space with low success rates. The fraction of real quasars with successful fits drops in the transition area between the high and low success rates of the simulation, suggesting that the present simulation reproduces the behavior of the real quasar hosts reasonably well.

The next question is how accurately the host galaxy brightness is measured for those real quasars with successful fits. We extract the simulated quasars in the parameter subspace where most of the real quasars with successful fits are found, i.e., $0.2 < z < 0.6$, $17.5 < i_0 < 21.5$, $0.5 < g_0 - i_0 < 2.5$, and $-2.0 < i_0 - i_0^{\text{QSO}} < 2.0$, and compare the input and output magnitudes (m_0 and m) of the host galaxies. The results are shown in Figure 9. The two sets of magnitudes are fairly consistent with each other, with systematic offsets and rms scatters measured to be $\langle g - g_0 \rangle = -0.08 \pm 0.63$, $\langle r - r_0 \rangle = -0.02 \pm 0.55$, $\langle i - i_0 \rangle = +0.03 \pm 0.49$, and $\langle z - z_0 \rangle = +0.01 \pm 0.49$. The derived absolute magnitudes also show slight systematic offsets from their correct values, which we found are weakly correlated with quasar-to-galaxy contrast (shown in the bottom left panel of Figure 9). This is presumably caused by two competing effects; some of the galaxy light close to the nuclei can be attributed wrongly to the quasar component (making $^{0.3}M_i - ^{0.3}M_{i,0}$ positive), while quasar light contaminates into host galaxies more severely when the quasar-to-galaxy contrast is higher (making $^{0.3}M_i - ^{0.3}M_{i,0}$ negative). However, this systematic error is small compared to the accuracy on which our conclusions stand, and we will see that correcting for it as a function of the quasar-to-galaxy contrast has little effect on our conclusions. Similarly, the systematic error of the derived absolute color ($^{0.3}(g-i) - ^{0.3}(g-i)_0 = -0.07$ mag in median) is too small to affect any of our conclusions.

4. RESULTS

We show the quasar-to-galaxy contrasts and associated magnitude differences as a function of redshift and quasar luminosity for the real quasars in Figure 10. Here all the successful fitting results in each band are included, regardless of the good-fit criterion. The median values of the contrasts (quasar brightness relative to galaxy brightness) in the (u , g , r , i , z) bands are (28.4, 14.2, 7.3, 5.8, 5.1) in peak intensity ratios and (7.5, 4.0, 1.6, 1.2, 1.0) in integrated flux ratios, respectively. As expected, the contrast is significantly higher in the bluer bands. While its correlation with redshift is relatively weak, that with the quasar luminosity (corresponding to F_{Quasar}) is remarkably strong. The slopes at $M_i < -24$ mag are close to the vector of constant F_{Galaxy} , meaning that F_{Quasar} and F_{Galaxy} are primarily independent of each other. Hao et al. (2005) found a similar lack of correlation between nuclear and host luminosities for Seyfert galaxies at low redshifts ($z < 0.15$). In our sample, the correlations flatten out at the higher luminosity where the fitting starts to fail for the highest-contrast objects. Indeed, the actual contrasts would presumably be higher and bluer than estimated here if we had proper measurements of those highest-contrast objects. Although the SDSS PSF magnitudes are commonly used to quantify

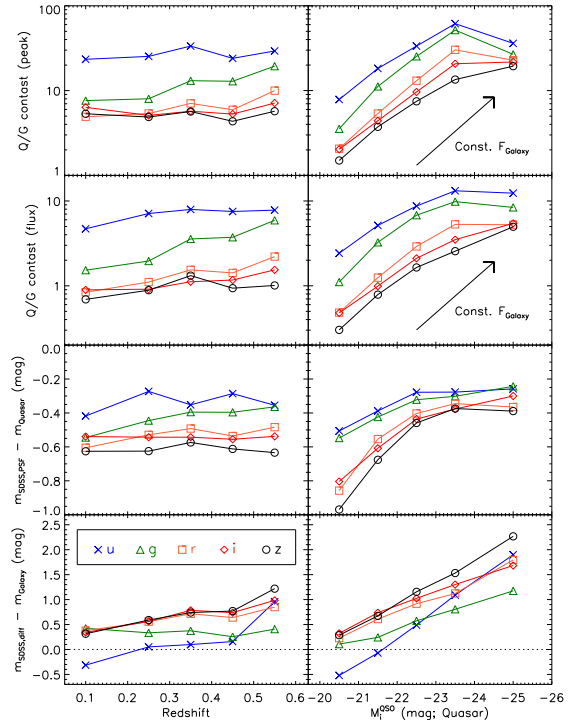


Figure 10. Quasar-to-galaxy contrasts and associated magnitude differences as a function of redshift and quasar absolute magnitude. The solid lines connected by crosses, triangles, squares, diamonds, and circles represent the u , g , r , i , and z bands, respectively. Top: median peak intensity ratios at the source center ($R < 1$ pixel). Second to top: median integrated flux ratios ($F_{\text{Quasar}}/F_{\text{Galaxy}}$). The arrows represent the vector of constant F_{Galaxy} . Third to top: difference between the SDSS PSF magnitudes ($m_{\text{SDSS,PSF}}$) and the decomposed quasar magnitudes (m_{Quasar}). Bottom: difference between $m_{\text{SDSS,diff}}$ (corresponding to the SDSS model flux minus the SDSS PSF flux) and the decomposed galaxy magnitudes (m_{Galaxy}).

the quasar brightness, they are found to be (0.33, 0.39, 0.51, 0.54, 0.61) mag brighter in median than the decomposed quasar magnitudes in the (u , g , r , i , z) bands. The systematic difference is larger for lower-luminosity quasars. On the other hand, the host brightness is sometimes approximated by the SDSS model flux minus the SDSS PSF flux. We convert this quantity into magnitude $m_{\text{SDSS,diff}}$, which is found to be (0.28, 0.33, 0.68, 0.82, 0.81) mag fainter than the decomposed galaxy magnitudes in median in the (u , g , r , i , z) bands. The discrepancy increases as the quasar luminosity increases.

Figure 11 shows the CMD of the host galaxies. The approximate stellar mass is shown on the upper axis, using the conversion described at the end of Section 3.1. The distribution of normal galaxies from the SDSS spectroscopic sample at $0.1 < z < 0.6$, taken from the MPA-JHU DR7 catalog⁶, is also shown for reference. We note that their redshift distribution is not well matched to that of the quasar host galaxies; about 80% of the reference sample is at $z < 0.3$ where very few of the quasar hosts are found. If we limit to $z > 0.3$, there is not a large and complete enough sample of normal galaxies in SDSS to serve as a good reference in this CMD. The median $^{0.3}M_i$ and $^{0.3}(g-i)$ values of the reference sample at each redshift are plotted in the figure. We also plot the MPA-

⁶ <http://www.mpa-garching.mpg.de/SDSS/>

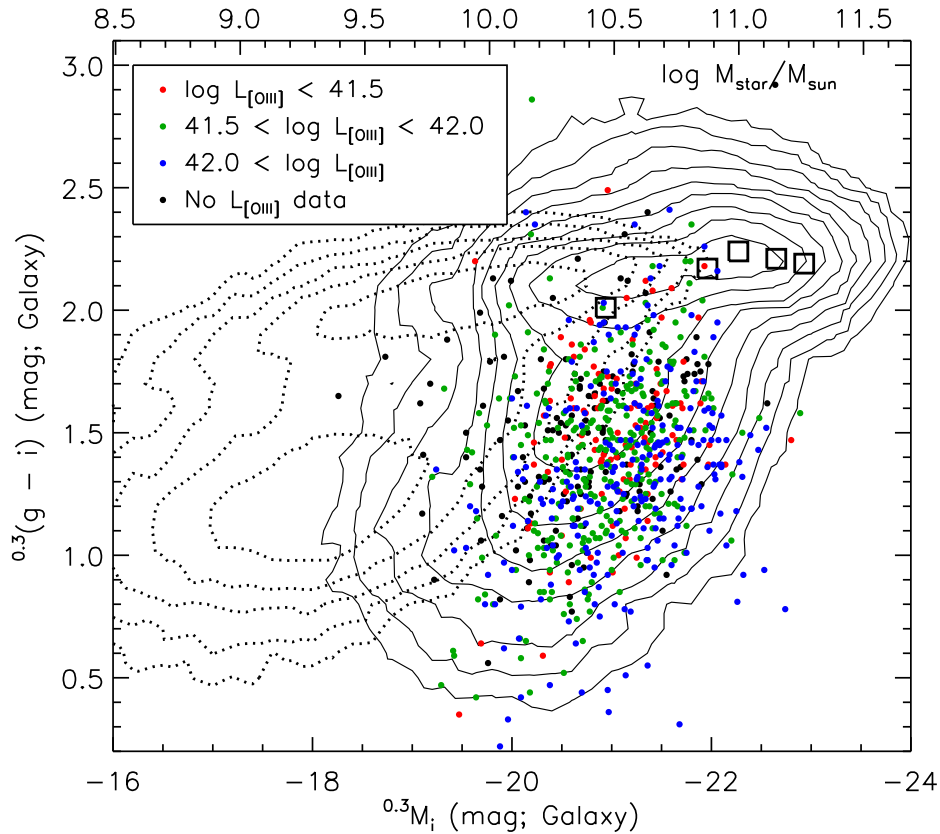


Figure 11. Color–magnitude diagram of the quasar hosts (dots) compared to normal galaxies (contours). The red, green, and blue dots correspond to the [O III] luminosity of $L_{[\text{O III}]} < 10^{41.5} \text{ erg s}^{-1}$, $10^{41.5} \text{ erg s}^{-1} < L_{[\text{O III}]} < 10^{42.0} \text{ erg s}^{-1}$, and $L_{[\text{O III}]} > 10^{42.0} \text{ erg s}^{-1}$, respectively. The black dots represent objects with no $L_{[\text{O III}]}$ data. The dotted and solid contours show the distributions of the SDSS normal galaxies (see text) at $z < 0.05$ and $0.1 < z < 0.6$, respectively. They are drawn at logarithmically stepped levels of number density. The squares represent the median $^{0.3}M_i$ and $^{0.3}(g-i)$ values of the normal galaxies at $z = 0.1\text{--}0.2$, $0.2\text{--}0.3$, $0.3\text{--}0.4$, $0.4\text{--}0.5$, and $0.5\text{--}0.6$ from left to right. The approximate stellar mass ($\log M_{\text{star}}/M_{\odot}$) is shown along the upper axis.

JHU galaxies at lower redshifts ($z < 0.05$) in order to show the location of the blue cloud in the local universe (the blue cloud is not clear at higher redshifts due to the limited depth of SDSS). The hosts of our quasars occupy a unique location in this diagram; they are almost exclusively massive with $10^{10}M_{\odot} < M_{\text{star}} < 10^{11}M_{\odot}$, and have colors ranging from the blue cloud to below the bottom of the red sequence. Compared to the majority of the normal galaxies with similar stellar mass, those quasar hosts are forming stars much more efficiently. Although objects with different quasar power (measured by the [O III] $\lambda 5007$ luminosity $L_{[\text{O III}]}$) are well mixed with each other, there seems to be a slight offset between the higher- and lower- $L_{[\text{O III}]}$ objects. We will return to this issue later.

With the decomposed galaxy components in hand, we can also check the relation between the mass of SMBHs and the host luminosity (stellar mass). They are plotted in Figure 12. Although the data points show significant scatter, there is a clear positive correlation between the two quantities. Thus we have recovered the $M_{\text{BH}} - M_{\text{star}}$ relation in optically luminous quasars. The best-fit linear relation is

$$\log \frac{M_{\text{BH}}}{10^8 M_{\odot}} = 0.09 - 0.24 (^{0.3}M_i + 20), \quad (2)$$

or

$$\log \frac{M_{\text{BH}}}{10^8 M_{\odot}} = 0.03 + 0.60 \log \frac{M_{\text{star}}}{10^{10} M_{\odot}}. \quad (3)$$

Compared to the local $M_{\text{BH}} - M_{\text{star}}$ relation of quiescent galaxies (Haring & Rix 2004), those quasar hosts are found to be under-massive for a given SMBH mass. Considering that our fitting procedure tends to fail for less-luminous host galaxies, this trend may be even stronger than appears in Figure 12. As shown in the figure, this result hardly changes when we correct for the systematic errors of $^{0.3}M_i$ as a function of the measured quasar-to-galaxy contrast (see Section 3.2). However, the relation measured here could be subject to serious selection effects and other observational biases, as discussed below.

5. DISCUSSION

5.1. Quasar Light in Host Galaxies

The simulations we carried out in Section 3.2 show that the measured host galaxy magnitudes are only slightly biased. In this subsection we explore this further, by looking for trends in the observed data that might indicate contamination of the galaxy light from the quasar. There are two possible causes of such a contamination. One is imperfect nucleus/host decomposition of the source profile, due to the limited precision of the PSF estimation and/or the fact that the galaxy may not be perfectly fit by a Sersic profile. Our fits may tend to overestimate the Sersic component since the Sersic, with three parameters, has more flexibility to fit a given profile than does the PSF. On the other hand, if there is a compact stellar core at the galactic center on top of the Sersic

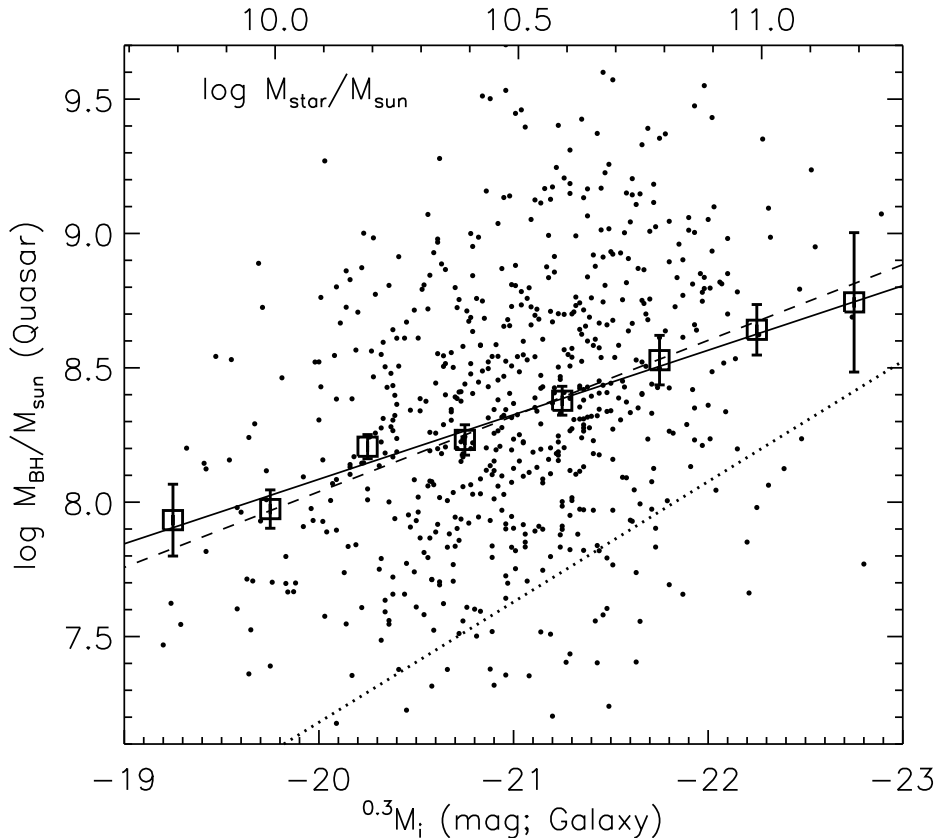


Figure 12. Relation between the mass of SMBHs and the host absolute magnitude $^{0.3}M_i$ of the quasars (black dots). The squares and the solid line represent the mean values and the best-fit linear relation, respectively. The dashed line shows the best-fit relation obtained when $^{0.3}M_i$ is corrected for its systematic error as a function of the measured quasar-to-galaxy contrast; this correction is very minor. The dotted line shows the local relation for quiescent galaxies (Håring & Rix 2004). The approximate stellar mass ($\log M_{\text{star}}/M_{\odot}$) is shown on the upper axis.

profile, such as a nuclear starburst, then it would be included in the PSF and lead to underestimation of the galaxy component. These two effects bias the measured host brightness in opposite directions. The other possible cause of the contamination is scattering of quasar light by the interstellar medium of the host galaxy. Unlike the first effect, this is an astrophysical effect and is an interesting subject in itself. Contamination of quasar light in the photometry of host galaxies, originating from either of these effects, would reveal itself most clearly in colors, since quasars are much bluer than galaxies in general. However, as we find in Figure 13, the color distributions of the decomposed quasars (PSF components) and host galaxies (Sérsic components) seem to be uncorrelated. The variation of the mean galaxy colors is only about ± 0.1 mag as the quasar colors change by 3 mag. Note that the slight positive correlation of the quasar and galaxy colors is expected, since our fitting analysis tends to fail for the bluest quasars with the reddest hosts due to high quasar-to-galaxy contrast in the g band. Furthermore, we have already seen that the magnitudes and colors of galaxies hosting the quasars with a range of [O III] luminosity are relatively well mixed (see Fig 11). These facts imply that quasar light contamination is not a large effect.

A straightforward way to check the effect of the imperfect nucleus/host decomposition is to compare the measured host properties of quasars with and without measurable nuclear contribution. To this end, we compare

the host magnitudes and colors of our sample to those of SDSS type-2 (obscured) quasars (Reyes et al. 2008) as shown in Figure 14. The redshifts of both samples are limited to $0.3 < z < 0.6$ (where most of our sample is located) for this comparison. The lack of type-2 quasars at low [O III] luminosity is due to the luminosity threshold imposed by Reyes et al. ($L_{[\text{OIII}]} \gtrsim 10^{41.9}$ erg s $^{-1}$). It is seen that the type-2 quasars are up to 0.5 mag more luminous than the hosts of type-1 objects. Since this excess brightness is higher at higher quasar luminosity, it may be due to quasar light scattered at the central part of the galaxy or nuclear starburst associated with AGN, which are included in the PSF component for the type-1 objects. If it has a stellar origin, then the magnitudes (stellar mass) of our quasar hosts could be underestimated by < 0.5 mag (< 0.2 dex). However, such a small reduction in host stellar mass doesn't change any of our conclusions significantly. On the other hand, the colors of the two types of quasars are almost perfectly consistent with each other, suggesting that our approach is very efficient in eliminating the nuclear contribution to host colors. The weak anti-correlation between the colors and [O III] luminosity can be explained by either AGN-associated star formation or scattered quasar light.

Currently the most reliable way to quantify the scattered quasar light is via polarimetric measurements. Based on the optical broadband- and spectro-polarimetric observations of SDSS type-2 quasars, Zakamska et al. (2005, 2006) confirmed the presence of

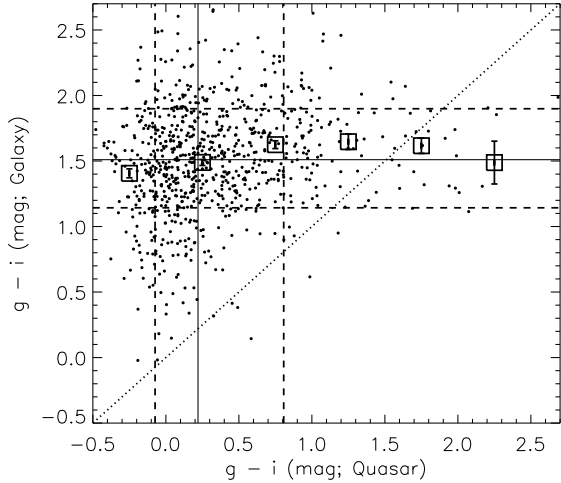


Figure 13. $g - i$ colors of the quasars (the PSF components) vs. those of the host galaxies (the Sérsic components). All the objects with successful fits in the g and i bands are included. The squares represent the mean values. The vertical and horizontal lines show the distribution of the quasar and galaxy colors, respectively; 68.3 % of the data points around the median value (solid line) are distributed between the two dashed lines. The dotted line shows the locus where the colors of the two components are identical.

significant amounts of scattered quasar light in host galaxies, and suggested a typical scattering efficiency of $\epsilon_{\text{sca}} \sim 1\%$. As a trial we re-calculated the absolute magnitudes and colors of our quasar hosts assuming $\epsilon_{\text{sca}} = 1\%$ (i.e., we subtracted 1 % of the decomposed PSF flux from the Sérsic flux before the k -correction), and found that the median values of $^{0.3}M_i$ and $^{0.3}(g - i)$ for the hosts change only by +0.01 and +0.02 mag, respectively. This is not surprising indeed, since the median quasar-to-galaxy contrasts of integrated flux are at most 4 in the g , r , i , and z bands; only 1 % of the quasar brightness cannot make a significant impact on the host brightness. In the extreme case of $\epsilon_{\text{sca}} = 10\%$, $^{0.3}M_i$ and $^{0.3}(g - i)$ would become larger than their original values by +0.10 mag and +0.21 mag, respectively. However, no compelling evidence for such a high scattering efficiency has been reported to date. Hence we conclude that the scattered quasar light has no significant impact on our results.

5.2. Massive Star-Forming Host Galaxies

Figure 11 demonstrates that the quasars of our sample are preferentially hosted by massive ($M_{\text{star}} > 10^{10} M_{\odot}$) galaxies with active star formation. Massive hosts have also been found for less luminous, narrow-line AGNs in the SDSS spectroscopic sample at lower redshifts ($z < 0.3$; Kauffmann et al. 2003). We note that our fitting analysis fails for about 23 % of the initial sample, most of which are too faint to give sufficient signal-to-noise ratios in the combined quasar and galaxy profiles. These faint sources could have systematically different host properties from those plotted in Figure 11. Nevertheless, we conclude that massive star-forming hosts are a common property of the majority, if not all, of low- z ($z < 0.6$) SDSS quasars. At lower luminosity ($M_u(z = 0.05) > -22$ mag) and lower redshifts ($z < 0.11$), Trump et al. (2013) reached a very similar conclusion to ours. Their method of AGN/host decomposition depends critically on the assumption that the AGN hosts have the same

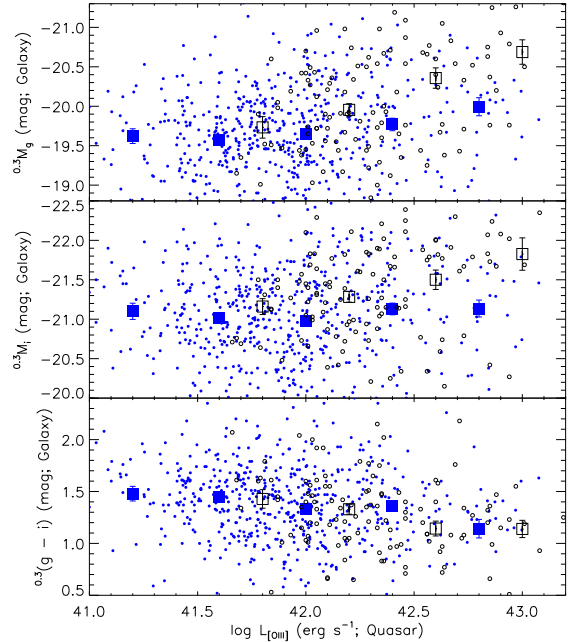


Figure 14. Absolute magnitudes $M_g^{0.3}$ (top), $M_i^{0.3}$ (middle) and colors $^{0.3}(g - i)$ (bottom) of quasar host galaxies as a function of [O III] $\lambda 5007$ luminosity. The dots and open circles represent the unobscured (type-1) quasars of this work and SDSS type-2 quasars (Reyes et al. 2008) at $0.3 < z < 0.6$, respectively. The filled and open squares represent the mean values of the type-1 and type-2 samples, respectively.

morphological structure as inactive galaxies on average, while our approach fit for the surface brightness profile of the hosts directly.

It is obvious that our conclusions do not apply to any quasar populations that are not included in the SDSS sample. However, the completeness of the SDSS selection for unobscured quasars is estimated to be fairly high; Vanden Berk et al. (2005) reported an overall completeness of about 89 % or higher to a limiting magnitude of $i = 19.1$ mag (corresponding to the limiting magnitude of the SDSS-I selection for low- z quasars; see also Richards et al. 2006). Furthermore, Stripe 82 has been observed for quasars more completely than any other area of the SDSS coverage using a variety of variability and color selection algorithms (Ross et al. 2012; Palanque-Delabrouille et al. 2011, 2013). Hence our conclusions may be generalized to all those unobscured quasars whose luminosity and redshifts are covered by the present sample.

Previous studies of narrow-line AGNs at low redshifts ($z < 0.3$, e.g., Kauffmann et al. 2003; Salim et al. 2007; Schawinski et al. 2010) have already found that the fraction of AGNs is higher in the blue cloud and the green valley than in the red sequence on the CMD. Kauffmann et al. (2003) found that the hosts of their low-luminosity type-2 AGNs have similar stellar content to normal early-type galaxies, while those of the high-luminosity AGNs have much younger stellar populations. Salim et al. (2007) reported that the hosts of the most powerful AGNs in their sample have comparable stellar mass and star formation rates (SFRs) to galaxies at the massive end of the blue cloud, while those of the weaker AGNs have considerably lower SFRs, extending into the red sequence. Our finding of almost

no quasar hosts on the red sequence is consistent with these results, as the quasars are an-order-of-magnitude higher-luminosity (measured by $L_{[\text{OIII}]}$) counterparts to the narrow-line AGNs studied by the above authors. The bluer hosts of more active AGNs might point to the presence of AGN-induced star formation predicted in numerical simulations (Wagner et al. 2012, 2013).

On the other hand, studies of optically faint X-ray AGNs at redshifts similar to or larger than those of our sample (up to $z \sim 1$) have found that their hosts are preferentially in the green valley and the red sequence (e.g., Nandra et al. 2007; Georgakakis et al. 2008; Silverman et al. 2008). This may suggest that different AGN types are hosted by different types of galaxies. If the optically luminous quasars and X-ray AGNs are on a single evolutionary path of hosts transiting from the blue cloud to the red sequence, then our result might suggest that optically luminous quasars precede X-ray AGNs in an evolutionary sequence (see also Shen et al. 2007; Hickox et al. 2009; Goulding et al. 2013). According to the merger-driven co-evolution scenario of galaxies and SMBHs (Hopkins et al. 2006), interactions/mergers of gas-rich galaxies first activate star formation and AGN, and then produce a dust-obscured, IR-luminous phase sometimes observed as ULIRGs. The narrow-line AGN phase may then follow. The systems further go into an optically luminous quasar phase when the dust is expelled by radiation pressure and the active nuclei become visible, and finally migrate into the red sequence as quasar and star-forming activity fades away. The blue host colors we found support the idea that quasars coincide with active star formation in host galaxies. Although the quasar-driven quenching of star formation (negative AGN feedback) has been proposed by many authors, such a process never becomes apparent in stellar properties during the most optically-luminous (i.e., quasar) phase of AGNs.

Some authors suggest that the apparent clustering of AGN hosts in the green valley and the red sequence is due to selection effects; if one works with a stellar mass-limited sample instead of a flux-limited sample, then the AGN fraction in the blue cloud would become comparably high to other regions of the CMD (Silverman et al. 2009; Xue et al. 2010). In addition, Cardamone et al. (2010) argue that most of the green AGN hosts have colors consistent with dusty star-forming galaxies and their intrinsic (dust-corrected) colors are located in the blue cloud. These studies point to a larger fraction of blue hosts than previously thought for obscured AGNs. If the above effects are also present in our analysis, then it would further strengthen our conclusion that quasar hosts are bluer and forming stars more efficiently than are the majority of normal galaxies.

In Figure 15, we plot the host colors versus the quasar Eddington ratios (R_{Edd}) in order to further investigate the possible interrelation between nuclear and star-forming activity. Very roughly speaking, the vertical axis corresponds to -2.5 times the logarithm of specific SFR ($-2.5 \log [\text{SFR}/M_{\text{star}}]$) with a constant offset since $\log \text{SFR} \approx \log (\text{UV luminosity}) = -0.4 \text{ }^{0.3}M_g + \text{constant}$ and $\log M_{\text{star}} \approx \log (\text{red optical/NIR luminosity}) = -0.4 \text{ }^{0.3}M_i + \text{constant}$. If one assumes that the $M_{\text{BH}} - M_{\text{star}}$ relation holds at every epoch of galaxy evo-

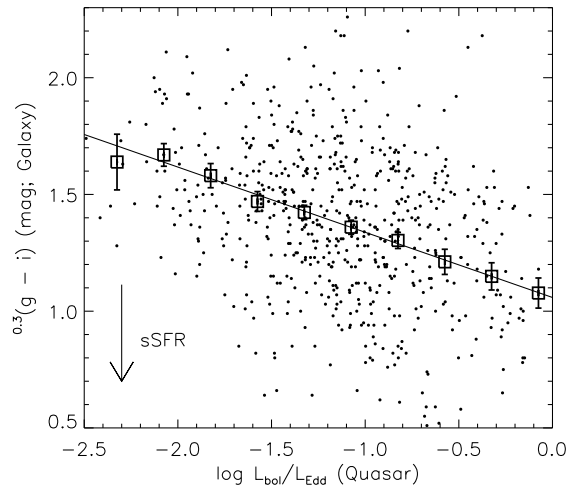


Figure 15. Host color vs. Eddington ratio of the quasars (dots). The mean values and the best-fit linear relation are represented by the squares and the solid line, respectively. Specific SFR increases toward the bottom of this plot.

lution (i.e., $M_{\text{BH}}(t) \propto M_{\text{star}}(t)$ at every time t), then

$$\text{sSFR}(t) = \frac{\dot{M}_{\text{star}}(t)}{M_{\text{star}}(t)} = \frac{\dot{M}_{\text{BH}}(t)}{M_{\text{BH}}(t)} \propto R_{\text{Edd}}(t). \quad (4)$$

The Eddington ratio and sSFR do show a positive correlation in Figure 15, but the slope is much shallower than expected from Equation (4); sSFR only doubles ($0.3(g-i)$ increases by about 0.7) as R_{Edd} increases by more than a factor of 100. This implies that the rise and fall of AGN and star formation are not precisely synchronized, although the assembly of SMBH and host stars keep pace with each other when averaged over time.

5.3. $M_{\text{BH}} - M_{\text{star}}$ Relation

Figure 12 demonstrates that the hosts of the SDSS quasars are under-massive for a given SMBH mass compared to the local relation. The discrepancy becomes larger at smaller mass, resulting in a shallow slope of the $M_{\text{BH}} - M_{\text{star}}$ relation. Such a systematic difference between the local relation and the relation we found could originate from various effects. The first is cosmological evolution during the time span of 5.7 Gyr between $z = 0.6$ and $z = 0.0$. However, we found little redshift evolution of the $M_{\text{BH}}/M_{\text{star}}$ ratio in the range probed by our sample ($0.1 \lesssim z < 0.6$) as shown in Figure 16. The ratio is offset from the local relation by the same amount even at $z < 0.3$, which casts doubt on the interpretation that the offset is due entirely to evolutionary effects. The second is an intrinsic difference between active and quiescent galaxies; although the M_{BH} estimators of active SMBHs are calibrated so that the local AGNs fall on the $M_{\text{BH}} - M_{\text{star}}$ relation of local quiescent galaxies, it is not clear whether the calibration remains robust at the higher-redshift universe. The third is selection effects and observational biases, as we now discuss.

Previous studies of the relation between M_{BH} and M_{star} (or the central stellar dispersion σ_* or the spheroidal mass M_{sph}) beyond the local universe are still very controversial. Many observations at $z < 1$ (e.g., Treu et al. 2004; Woo et al. 2006, 2008; Canalizo et al. 2012) and beyond (e.g., Peng et al. 2006; Shields et al. 2006; Bennert et al. 2011) even up to $z \sim 6$ (Walter et al.

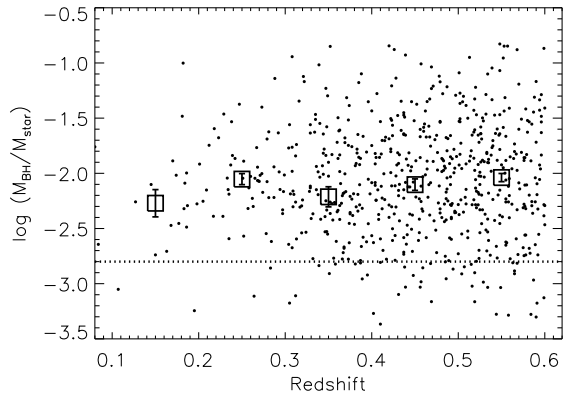


Figure 16. $M_{\text{BH}}/M_{\text{star}}$ ratio as a function of redshift (dots). The squares represent the mean of the sample. The dotted line represents the local relation of quiescent galaxies (Häring & Rix 2004).

2004; Wang et al. 2013) suggest that the $M_{\text{BH}}/M_{\text{sph}}$ ratio increases toward high redshift. Our results are qualitatively consistent with these studies, although our M_{star} includes not only a spheroid but also a disk component if it exists. Attempts have been made to quantify the evolution of the ratio in the form of $M_{\text{BH}}/M_{\text{sph}} \propto (1+z)^\gamma$, but γ varies significantly from paper to paper; for example, $\gamma = 2.07 \pm 0.76$ (measured at $0 < z < 2$; McLure et al. 2006), $\gamma = 0.68 \pm 0.12^{+0.6}_{-0.3}$ ($1 < z < 2.2$; Merloni et al. 2010), or $\gamma = 1.4 \pm 0.2$ ($0 < z < 4.5$; Bennert et al. 2010). If $M_{\text{BH}}/M_{\text{sph}}$ increases toward high redshift, this suggests that SMBHs grow, or are assembled, earlier than their host galaxies. However, other studies claim no such evolution. Shields et al. (2003) showed that the local $M_{\text{BH}} - \sigma_*$ relation holds up to $z \sim 3$. Using over 900 AGNs drawn from SDSS, Shen et al. (2008) also found no evolution of the $M_{\text{BH}} - \sigma_*$ relation at $z < 0.4$. Similar conclusions were reached for AGNs at $0.5 < z < 1.2$ by Schramm & Silverman (2013) and at $2 \lesssim z \lesssim 3$ by Adelberger & Steidel (2005).

At least some of the above controversy may be attributed to various observational biases (e.g., Salviander et al. 2007). In a flux-limited sample, quasar luminosity and M_{BH} are systematically larger in higher-redshift objects. If the $M_{\text{BH}} - M_{\text{star}}$ relation is not well calibrated at high masses in the local universe, then the $M_{\text{BH}}/M_{\text{star}}$ ratio would deviate systematically at high redshifts. If the single-epoch M_{BH} estimators are not accurately calibrated over a wide dynamic range of quasar luminosity, then it would also give rise to a redshift-dependent bias. Shen & Kelly (2010) demonstrated that the uncertainty in the single-epoch M_{BH} estimates could have a significant impact on the derived $M_{\text{BH}} - M_{\text{star}}$ relation. Various quality cuts used to select the sample may also result in a redshift-dependent bias. Furthermore, for a given galaxy mass, more massive SMBHs have higher chance of being selected if they tend to have higher AGN luminosity (Lauer et al. 2007). When coupled with a bottom-heavy galaxy mass function, this can produce a Malmquist-type bias and result in a higher $M_{\text{BH}}/M_{\text{star}}$ ratio at higher redshifts (see also Shen 2013). A similar but different source of bias was pointed out by Schulze & Wisotzki (2011), in which the decreasing fraction of active SMBHs at higher mass results in a larger fraction of lower-mass SMBHs being selected at fixed

bulge properties. They gave a comprehensive discussion of various selection biases and demonstrated that, while the observed departures of the $M_{\text{BH}}/M_{\text{bulge}}$ ratio from the local relation are sometimes very large at high redshifts, they could be all attributed to the accumulated effects of various selection biases. The fundamental problem is that our current knowledge about SMBHs beyond the local universe is necessarily based only on AGNs above a certain observed flux. We do not really know whether the points in Figure 12 are representative of, or just a part of the envelope of, the underlying distribution of all the (active and inactive) SMBHs at the relevant redshifts.

6. SUMMARY AND CONCLUSIONS

We have analyzed the photometric properties of galaxies hosting optically luminous, unobscured quasars at $z < 0.6$. The sample was selected from the fifth SDSS quasar catalog (Schneider et al. 2010) and the first BOSS quasar catalog (Pâris et al. 2012) on Stripe 82, where deep co-added SDSS images are available. Each quasar image is decomposed into nucleus and host galaxy using the PSF and the Sérsic models. 802 objects (77 % of the initially selected sample) are successfully fitted with our approach in at least three of the g , r , i , and z bands, which constitute our final sample. We confirmed that the effect of quasar light contamination due to the imperfect nucleus/host decomposition is not very large. The systematic errors in the measured galaxy absolute magnitudes and colors are estimated to be less than 0.5 mag and 0.1 mag, respectively, with simulated quasar images. Scattered quasar light cannot affect host brightness as long as the scattering efficiency is about 1 % or less. Our main conclusions are as follows.

1. The SDSS quasars are almost exclusively hosted by massive galaxies with $M_{\text{star}} > 10^{10} M_\odot$. This is consistent with the results of previous studies on less luminous, narrow-line AGNs. The quasar hosts are also very blue and almost absent on the red sequence, which is in stark contrast to the color-magnitude distribution of normal galaxies. The fact that more active AGNs reside in bluer galaxies may suggest that negative AGN feedback, if it exists, is not concurrent with the most optically luminous phase of AGN.
2. There is a positive correlation between M_{BH} and M_{star} of the SDSS quasars. However, the $M_{\text{BH}} - M_{\text{star}}$ relation is offset toward larger M_{BH} or smaller M_{star} compared to the local relation. While this could indicate that SMBHs are assembled or grow earlier than their host galaxies, we argue that it is not clear whether the sample is representative of the whole active and inactive SMBHs at the relevant redshifts due to various observational biases.

The present work demonstrates that luminosity and colors of quasar host galaxies can be extracted from optical multi-band images with moderate spatial resolution. We will expand the analysis into higher redshifts and lower luminosity with the wide-field imaging data obtained in the coming Subaru/Hyper Suprime-Cam (HSC) survey, which is scheduled to start in early 2014. The Wide layer of the HSC survey plans to observe 1400 deg^2

of the SDSS footprint with an expected depth of $i = 25.9$ mag (5σ , $2''$ aperture) and a PSF full width at half maximum of less than $0''.7$. Thus these data will significantly supersede SDSS both in depth and image quality.

We are grateful to Jenny Greene and Yue Shen for fruitful discussions and suggestions. We thank an anonymous referee for his/her very useful comments. This work was supported by Grants-in-Aid for Young Scientists (A) (22684995) and for Scientific Research on Innovative Areas (24111705) from the Japan Society for the Promotion of Science (JSPS). YM was a JSPS research fellow during part of this work and was supported by a Grant-in-Aid for JSPS Fellows (SPD, 25-1646).

Funding for the SDSS and SDSS-II has been provided by the Alfred P. Sloan Foundation, the Participating Institutions, the National Science Foundation, the U.S. Department of Energy, the National Aeronautics and Space Administration, the Japanese Monbukagakusho, the Max Planck Society, and the Higher Education Funding Council for England. The SDSS Web site is <http://www.sdss.org/>.

The SDSS is managed by the Astrophysical Research Consortium for the Participating Institutions. The Participating Institutions are the American Museum of Natural History, Astrophysical Institute Potsdam, University of Basel, University of Cambridge, Case Western Reserve University, University of Chicago, Drexel University, Fermilab, the Institute for Advanced Study, the Japan Participation Group, Johns Hopkins University, the Joint Institute for Nuclear Astrophysics, the Kavli Institute for Particle Astrophysics and Cosmology, the Korean Scientist Group, the Chinese Academy of Sciences (LAMOST), Los Alamos National Laboratory, the Max-Planck-Institute for Astronomy (MPIA), the Max-Planck-Institute for Astrophysics (MPA), New Mexico State University, Ohio State University, University of Pittsburgh, University of Portsmouth, Princeton University, the United States Naval Observatory, and the University of Washington.

Funding for SDSS-III has been provided by the Alfred P. Sloan Foundation, the Participating Institutions, the National Science Foundation, and the U.S. Department of Energy Office of Science. The SDSS-III Web site is <http://www.sdss3.org/>.

SDSS-III is managed by the Astrophysical Research Consortium for the Participating Institutions of the SDSS-III Collaboration including the University of Arizona, the Brazilian Participation Group, Brookhaven National Laboratory, University of Cambridge, Carnegie Mellon University, University of Florida, the French Participation Group, the German Participation Group, Harvard University, the Instituto de Astrofísica de Canarias, the Michigan State/Notre Dame/JINA Participation Group, Johns Hopkins University, Lawrence Berkeley National Laboratory, Max Planck Institute for Astrophysics, Max Planck Institute for Extraterrestrial Physics, New Mexico State University, New York University, Ohio State University, Pennsylvania State University, University of Portsmouth, Princeton University, the Spanish Participation Group, University of Tokyo, University of Utah, Vanderbilt University, University of Virginia, University of Washington, and Yale University.

REFERENCES

- Abazajian, K. N., Adelman-McCarthy, J. K., Agüeros, M. A., et al. 2009, *ApJS*, 182, 543
- Adelberger, K. L., & Steidel, C. C. 2005, *ApJ*, 627, L1
- Ahn, C. P., Alexandroff, R., Allende Prieto, C., et al. 2013, [arXiv:1307.7735](https://arxiv.org/abs/1307.7735)
- Ahn, C. P., Alexandroff, R., Allende Prieto, C., et al. 2012, *ApJS*, 203, 21
- Annis, J., Soares-Santos, M., Strauss, M. A., et al. 2011, [arXiv:1111.6619](https://arxiv.org/abs/1111.6619)
- Antonucci, R. 1993, *ARA&A*, 31, 473
- Bahcall, J. N., Kirhakos, S., Saxe, D. H., & Schneider, D. P. 1997, *ApJ*, 479, 642
- Barnes, J. E., & Hernquist, L. E. 1991, *ApJ*, 370, L65
- Bennert, V. N., Auger, M. W., Treu, T., Woo, J.-H., & Malkan, M. A. 2011, *ApJ*, 742, 107
- Bennert, V. N., Treu, T., Woo, J.-H., et al. 2010, *ApJ*, 708, 1507
- Blanton, M. R., & Roweis, S. 2007, *AJ*, 133, 734
- Boroson, T. A., & Oke, J. B. 1982, *Nature*, 296, 397
- Bower, R. G., Benson, A. J., Malbon, R., et al. 2006, *MNRAS*, 370, 645
- Brotherton, M. S., Grabelsky, M., Canalizo, G., et al. 2002, *PASP*, 114, 593
- Brotherton, M. S., van Breugel, W., Stanford, S. A., et al. 1999, *ApJ*, 520, L87
- Canalizo, G., Wold, M., Hiner, K. D., et al. 2012, *ApJ*, 760, 38
- Cano-Díaz, M., Maiolino, R., Marconi, A., et al. 2012, *A&A*, 537, L8
- Cardamone, C. N., Urry, C. M., Schawinski, K., et al. 2010, *ApJ*, 721, L38
- Ciotti, L., & Ostriker, J. P. 2007, *ApJ*, 665, 1038
- Dawson, K. S., Schlegel, D. J., Ahn, C. P., et al. 2013, *AJ*, 145, 10
- Choi, J.-H., & Nagamine, K. 2011, *MNRAS*, 410, 2579
- Croton, D. J., Springel, V., White, S. D. M., et al. 2006, *MNRAS*, 365, 11
- Davé, R., Oppenheimer, B. D., & Finlator, K. 2011, *MNRAS*, 415, 11
- Di Matteo, T., Springel, V., & Hernquist, L. 2005, *Nature*, 433, 604
- Dressler, A. 1989, *Active Galactic Nuclei: proceedings of IAUS 134*, held in Santa Cruz, California, August 15-19, 1988. Edited by Donald E. Osterbrock and Joseph S. Miller. IAUS 134, Kluwer Academic Publishers, Dordrecht, p.217
- Elitzur, M. 2012, *ApJ*, 747, L33
- Fabian, A. C. 2012, *ARA&A*, 50, 455
- Ferrarese, L., & Merritt, D. 2000, *ApJ*, 539, L9
- Feruglio, C., Maiolino, R., Piconcelli, E., et al. 2010, *A&A*, 518, L155
- Frieman, J. A., Bassett, B., Becker, A., et al. 2008, *AJ*, 135, 338
- Fu, H., & Stockton, A. 2009, *ApJ*, 690, 953
- Gebhardt, K., Bender, R., Bower, G., et al. 2000, *ApJ*, 539, L13
- Georgakakis, A., Nandra, K., Yan, R., et al. 2008, *MNRAS*, 385, 2049
- Graham, A. W., & Driver, S. P. 2005, *PASA*, 22, 118
- Greene, J. E., Zakamska, N. L., Ho, L. C., & Barth, A. J. 2011, *ApJ*, 732, 9
- Goulding, A. D., Forman, W. R., Hickox, R. C., et al. 2013, [arXiv:1310.8298](https://arxiv.org/abs/1310.8298)
- Gültekin, K., Richstone, D. O., Gebhardt, K., et al. 2009, *ApJ*, 698, 198
- Gunn, J. E., Carr, M., Rockosi, C., et al. 1998, *AJ*, 116, 3040
- Gunn, J. E., Siegmund, W. A., Mannery, E. J., et al. 2006, *AJ*, 131, 2332
- Hao, L., Strauss, M. A., Fan, X., et al. 2005, *AJ*, 129, 1795
- Håring, N., & Rix, H.-W. 2004, *ApJ*, 604, L89
- Hickox, R. C., Jones, C., Forman, W. R., et al. 2009, *ApJ*, 696, 891
- Hopkins, P. F., Hernquist, L., Cox, T. J., et al. 2006, *ApJS*, 163, 1
- Husemann, B., Sánchez, S. F., Wisotzki, L., et al. 2010, *A&A*, 519, A115
- Ivezić, Ž., Smith, J. A., Miknaitis, G., et al. 2007, *AJ*, 134, 973
- Kauffmann, G., Heckman, T. M., Tremonti, C., et al. 2003, *MNRAS*, 346, 1055
- Jahnke, K., Sánchez, S. F., Wisotzki, L., et al. 2004, *ApJ*, 614, 568
- Jahnke, K., Wisotzki, L., Courbin, F., & Letawe, G. 2007, *MNRAS*, 378, 23

- Keel, W. C., Chojnowski, S. D., Bennert, V. N., et al. 2012, *MNRAS*, 420, 878
- Kirhakos, S., Bahcall, J. N., Schneider, D. P., & Kristian, J. 1999, *ApJ*, 520, 67
- Kormendy, J. 1993, *The Nearest Active Galaxies*, Proceedings of the meeting on The nearest active galaxies, held in Madrid in May 1992, Madrid: Consejo Superior de Investigaciones Cientificas, 1993, Edited by J. Beckman, L. Colina and H. Netzer, p. 197
- Kormendy, J., & Ho, L. C. 2013, *ARA&A*, 51, 511
- Kotilainen, J. K., & Ward, M. J. 1994, *MNRAS*, 266, 953
- Lauer, T. R., Tremaine, S., Richstone, D., & Faber, S. M. 2007, *ApJ*, 670, 249
- Liu, G., Zakamska, N. L., Greene, J. E., Nesvadba, N. P. H., & Liu, X. 2013b, arXiv:1305.6922
- Liu, G., Zakamska, N. L., Greene, J. E., Nesvadba, N. P. H., & Liu, X. 2013a, *MNRAS*, 430, 2327
- Liu, X., Zakamska, N. L., Greene, J. E., et al. 2009, *ApJ*, 702, 1098
- Lupton, R., Blanton, M. R., Fekete, G., et al. 2004, *PASP*, 116, 133
- Lupton, R., Gunn, J. E., Ivezić, Z., Knapp, G. R., & Kent, S. 2001, *Astronomical Data Analysis Software and Systems X*, 238, 269
- Magorrian, J., Tremaine, S., Richstone, D., et al. 1998, *AJ*, 115, 2285
- Matsuoka, Y. 2012, *ApJ*, 750, 54
- McLure, R. J., Kukula, M. J., Dunlop, J. S., et al. 1999, *MNRAS*, 308, 377
- McLure, R. J., & Dunlop, J. S. 2002, *MNRAS*, 331, 795
- McLure, R. J., Jarvis, M. J., Targett, T. A., Dunlop, J. S., & Best, P. N. 2006, *MNRAS*, 368, 1395
- McNamara, B. R., & Nulsen, P. E. J. 2007, *ARA&A*, 45, 117
- Merloni, A., Bongiorno, A., Bolzonella, M., et al. 2010, *ApJ*, 708, 137
- Merritt, D., & Ferrarese, L. 2001, *MNRAS*, 320, L30
- Nandra, K., Georgakakis, A., Willmer, C. N. A., et al. 2007, *ApJ*, 660, L11
- Nesvadba, N. P. H., Lehnert, M. D., Eisenhauer, F., et al. 2006, *ApJ*, 650, 693
- Ostriker, J. P., Choi, E., Ciotti, L., Novak, G. S., & Proga, D. 2010, *ApJ*, 722, 642
- Palanque-Delabrouille, N., Magneville, C., Yèche, C., et al. 2013, *A&A*, 551, A29
- Palanque-Delabrouille, N., Yèche, C., Myers, A. D., et al. 2011, *A&A*, 530, A122
- Pâris, I., Petitjean, P., Aubourg, É., et al. 2012, *A&A*, 548, A66
- Peng, C. Y., Impey, C. D., Rix, H.-W., et al. 2006, *ApJ*, 649, 616
- Reyes, R., Zakamska, N. L., Strauss, M. A., et al. 2008, *AJ*, 136, 2373
- Richards, G. T., Strauss, M. A., Fan, X., et al. 2006, *AJ*, 131, 2766
- Rönnback, J., van Groningen, E., Wanders, I., Örn Dahl, E. 1996, *MNRAS*, 283, 282
- Ross, N. P., Myers, A. D., Sheldon, E. S., et al. 2012, *ApJS*, 199, 3
- Salim, S., Rich, R. M., Charlot, S., et al. 2007, *ApJS*, 173, 267
- Salviander, S., Shields, G. A., Gebhardt, K., & Bonning, E. W. 2007, *ApJ*, 662, 131
- Sánchez, S. F., Jahnke, K., Wisotzki, L., et al. 2004, *ApJ*, 614, 586
- Sanders, D. B., Soifer, B. T., Elias, J. H., et al. 1988, *ApJ*, 325, 74
- Schawinski, K., Urry, C. M., Virani, S., et al. 2010, *ApJ*, 711, 284
- Schlegel, D. J., Finkbeiner, D. P., & Davis, M. 1998, *ApJ*, 500, 525
- Schneider, D. P., Richards, G. T., Hall, P. B., et al. 2010, *AJ*, 139, 2360
- Schramm, M., & Silverman, J. D. 2013, *ApJ*, 767, 13
- Schulze, A., & Wisotzki, L. 2011, *A&A*, 535, A87
- Sersic, J. L. 1968, Cordoba, Argentina: Observatorio Astronomico, 1968
- Shen, J., Vanden Berk, D. E., Schneider, D. P., & Hall, P. B. 2008, *AJ*, 135, 928
- Shen, Y. 2013, *Bulletin of the Astronomical Society of India*, 41, 61
- Shen, Y., & Kelly, B. C. 2010, *ApJ*, 713, 41
- Shen, Y., & Liu, X. 2012, *ApJ*, 753, 125
- Shen, Y., Mulchaey, J. S., Raychaudhury, S., Rasmussen, J., & Ponman, T. J. 2007, *ApJ*, 654, L115
- Shen, Y., Richards, G. T., Strauss, M. A., et al. 2011, *ApJS*, 194, 45
- Shields, G. A., Gebhardt, K., Salviander, S., et al. 2003, *ApJ*, 583, 124
- Shields, G. A., Menezes, K. L., Massart, C. A., & Vanden Bout, P. 2006, *ApJ*, 641, 683
- Silverman, J. D., Lamareille, F., Maier, C., et al. 2009, *ApJ*, 696, 396
- Silverman, J. D., Mainieri, V., Lehmer, B. D., et al. 2008, *ApJ*, 675, 1025
- Smee, S. A., Gunn, J. E., Uomoto, A., et al. 2013, *AJ*, 146, 32
- Somerville, R. S., Hopkins, P. F., Cox, T. J., Robertson, B. E., & Hernquist, L. 2008, *MNRAS*, 391, 481
- Springel, V., Di Matteo, T., & Hernquist, L. 2005, *ApJ*, 620, L79
- Strauss, M. A., Weinberg, D. H., Lupton, R. H., et al. 2002, *AJ*, 124, 1810
- Treu, T., Malkan, M. A., & Blandford, R. D. 2004, *ApJ*, 615, L97
- Trump, J. R., Hsu, A. D., Fang, J. J., et al. 2013, *ApJ*, 763, 133
- Vanden Berk, D. E., Schneider, D. P., Richards, G. T., et al. 2005, *AJ*, 129, 2047
- Wagner, A. Y., Bicknell, G. V., & Umemura, M. 2012, *ApJ*, 757, 136
- Wagner, A. Y., Umemura, M., & Bicknell, G. V. 2013, *ApJ*, 763, L18
- Walter, F., Carilli, C., Bertoldi, F., et al. 2004, *ApJ*, 615, L17
- Wang, R., Wagg, J., Carilli, C. L., et al. 2013, *ApJ*, 773, 44
- Woo, J.-H., Treu, T., Malkan, M. A., & Blandford, R. D. 2008, *ApJ*, 681, 925
- Woo, J.-H., Treu, T., Malkan, M. A., & Blandford, R. D. 2006, *ApJ*, 645, 900
- Xue, Y. Q., Brandt, W. N., Luo, B., et al. 2010, *ApJ*, 720, 368
- York, D. G., Adelman, J., Anderson, J. E., Jr., et al. 2000, *AJ*, 120, 1579
- Zakamska, N. L., Schmidt, G. D., Smith, P. S., et al. 2005, *AJ*, 129, 1212
- Zakamska, N. L., Strauss, M. A., Krolik, J. H., et al. 2006, *AJ*, 132, 1496
- Zakamska, N. L., Strauss, M. A., Krolik, J. H., et al. 2003, *AJ*, 126, 2125